RSC Advances

PAPER

View Article Online
View Journal | View Issue

Cite this: *RSC Adv.*, 2020, **10**, 36090

O_2 activation by core–shell $Ru_{13}@Pt_{42}$ particles in comparison with Pt_{55} particles: a DFT study†

Jing Lu,[a] Bo Zhu [b] and Shigeyoshi Sakaki *[bc]

The reaction of O_2 with a $Ru_{13}@Pt_{42}$ core–shell particle consisting of a Ru_{13} core and a Pt_{42} shell was theoretically investigated in comparison with Pt_{55}. The O_2 binding energy with Pt_{55} is larger than that with $Ru_{13}@Pt_{42}$, and O–O bond cleavage occurs more easily with a smaller activation barrier (E_a) on Pt_{55} than on $Ru_{13}@Pt_{42}$. Protonation to the Pt_{42} surface followed by one-electron reduction leads to the formation of an H atom on the surface with considerable exothermicity. The H atom reacts with the adsorbed O_2 molecule to afford an OOH species with a larger E_a value on Pt_{55} than on $Ru_{13}@Pt_{42}$. An OOH species is also formed by protonation of the adsorbed O_2 molecule, followed by one-electron reduction, with a large exothermicity in both Pt_{55} and $Ru_{13}@Pt_{42}$. O–OH bond cleavage occurs with a smaller E_a on Pt_{55} than on $Ru_{13}@Pt_{42}$. The lower reactivity of $Ru_{13}@Pt_{42}$ than that of Pt_{55} on the O–O and O–OH bond cleavages arises from the presence of lower energy in the d-valence band-top and d-band center in $Ru_{13}@Pt_{42}$ than in Pt_{55}. The smaller E_a for OOH formation on $Ru_{13}@Pt_{42}$ than on Pt_{55} arises from weaker $Ru_{13}@Pt_{42}$–O_2 and $Ru_{13}@Pt_{42}$–H bonds than the Pt_{55}–O_2 and Pt_{55}–H bonds, respectively. The low-energy d-valence band-top is responsible for the weak $Ru_{13}@Pt_{42}$–O and $Ru_{13}@Pt_{42}$–OH bonds. Thus, the low-energy d-valence band-top and d-band center are important properties of the $Ru_{13}@Pt_{42}$ particle.

Received 1st July 2020
Accepted 3rd September 2020

DOI: 10.1039/d0ra05738j

rsc.li/rsc-advances

1. Introduction

The proton exchange membrane fuel cell (PEMFC) is a promising candidate for a clean and sustainable energy source to cope with the growing energy consumption and related environmental concerns. Pt particles are used as a catalyst for the oxygen reduction reaction (ORR) at the PEMFC cathode because of their incomparable catalytic activity and stability in acidic solution, as discussed in recent reviews;[1–6] we cite here reviews from the last 5 years because many reviews have been published. However, their limited availability on earth and high cost still remain major obstacles for the wide use of PEMFCs. One of the promising methods to solve this problem is the use of core–shell Pt particles (M@Pt) consisting of Pt for the shell and abundant metals (M) for the core, because Pt content can be reduced in the catalyst by the use of a M core but the Pt shell exhibits high catalytic activity and stability in acid solution, as reviewed in the last few years.[7–14] Also, one can expect to improve the catalytic activity of the Pt shell by tuning the electronic structure of the Pt shell with the M core.

Recently, core–shell Ru@Pt particles have been reported as excellent ORR catalysts.[15–20] For instance, Adzic and co-workers demonstrated that the catalytic activity of Ru@Pt could be tuned by varying the Pt shell thickness; $Ru@Pt_{2ML}$ with two Pt layers was more active than $Ru@Pt_{xML}$ ($x = 1$ and 3).[15] Jackson and coworkers[17,19] and Takimoto and coworkers[18] reported that the catalytic activity of Ru@Pt for the ORR exceeded that of a commercial Pt electrode. Jackson and co-workers also interestingly obtained a volcano plot of the catalytic activity against the O binding energy, suggesting that both overly strong and overly weak O binding with the Pt surface is not good for ORR catalysts.[17] However, the relation between electronic structure and origin of the O binding energy has been unclear.

Many theoretical ORR studies reported so far discuss the relation between electronic structure of the catalyst and ORR activity.[21–39] In particular, the O–O bond activation has been

[a]*Hubei Key Laboratory of Advanced Textile Materials & Application, Hubei International Scientific and Technological Cooperation Base of Intelligent Textile Materials & Application, Wuhan Textile University, Wuhan 430200, China*

[b]*Element Strategy Initiative for Catalysts and Batteries, Kyoto University, Goryo-Ohara 1-30, Nishikyo-ku, Kyoto 615-8245, Japan. E-mail: sakaki.shigeyoshi.47e@st.kyoto-u.ac.jp; Fax: +81-75-383-3047; Tel: +81-75-383-3036*

[c]*Fukui Institute for Fundamental Chemistry (FIFC), Kyoto University, Takano-Nishihiraki-cho 34-4, Sakyou-ku, Kyoto 606-8103, Japan*

† Electronic supplementary information (ESI) available: Possible adsorption structures of 2(O) species and (O)(OH) species (Scheme S1); total energies for Pt_{55} and $Pt_{42}Ru_{13}$ in different possible spin states using PBE-D3 method (Table S1); binding energies (E_b, in eV) for O_2 and OOH species (Table S2); binding energies (E_b, in eV) for O, OH, and H/x-binding species (Table S3); optimized structures of O_2-binding species (Fig. S1), 2O-binding species (Fig. S2), OOH-binding species (Fig. S3), (O)(OH)-binding species (Fig. S4) and Cartesian coordinates of important optimized species discussed in the main text. The effect of box size for periodic calculation on the Fermi level ($\varepsilon_{F,\ eV}$) and the d-valence band top ($\varepsilon_{VB\_top,\ eV}$) energies (Table S4). d-Valence band top energy (in eV) calculated using several different functionals and basis sets (Table S5). See DOI: 10.1039/d0ra05738j

theoretically investigated in many works, as discussed by a recent review[40] and many works even after this review.[41–46] However, the theoretical study of Ru@Pt has been limited so far; for instance, the O and OH-binding energies with Ru_{13}@Pt_{42} and Pt_{55} have been theoretically investigated,[47] but the O–O bond cleavage on Ru@Pt has not been investigated, despite the crucial importance of such O–O bond cleavage in the ORR. Considering that the theoretical study of nanoscale metal particles is still challenging and its development is needed even currently,[48–50] the theoretical study of the O_2 reaction on Ru@Pt and related metal particles is indispensable.

In this work, we theoretically investigated dioxygen (O_2) adsorption and O–O bond cleavage by the Ru_{13}@Pt_{42} particle in comparison with the Pt_{55} particle using DFT computations. In the O–O bond cleavage, two reaction courses are plausible; in one, the O–O bond of the adsorbed O_2 molecule is cleaved. In the other reaction course, OOH species are formed on the surface, followed by O–OH bond cleavage, because it is likely that the OOH species are easily formed in the presence of excess protons and enough supply of electrons to the electrode. Our purposes here are to explore O_2 adsorption, O–O bond cleavage, OOH formation, and O–OH bond cleavage, compare the reactivity between Ru_{13}@Pt_{42} and Pt_{55}, find important factor(s) determining the reactivities of Ru_{13}@Pt_{42} and Pt_{55}, and present a theoretical understanding of the differences between Ru_{13}@Pt_{42} and Pt_{55}. We believe that the theoretical findings on these issues are valuable for understanding the chemistry of nanometal particles.

2. Computational methods and models

Spin-polarized periodic DFT calculations were carried out using the Vienna *Ab initio* Simulation Package (VASP),[51,52] where plane-wave basis sets were employed with an energy cutoff of 400 eV, and the projector-augmented-wave (PAW) pseudopotentials were used to represent core electrons. The PBE-D3 functional was employed in all calculations,[53] where "D3" represents the dispersion correction proposed by Grimme's group.[54,55] Ru@Pt and Pt particles were placed in a large supercell (25 Å × 25 Å × 25 Å) to ensure enough separation by vacuum. Geometry optimization of equilibrium structure was carried out in gas phase using the energy threshold of 0.0001 eV and force threshold of 0.01 eV $Å^{-1}$. Optimization of transition state (TS) was carried out using the climing image nudged elastic band (CI-NEB) method with the VASP transition-state tools (VTST),[56,57] in which thresholds for convergence were set to 0.0001 eV for energy and 0.02 eV $Å^{-1}$ for force. To evaluate solvent effects, an implicit solvation model, which describes the effect of electrostatic interaction between solute and solvent, was employed as implemented in VASPsol,[58,59] where optimized geometry in gas phase was used.

Though Pt_{55} and Ru_{13}@Pt_{42} particles are not very large compared to real catalysts, we employed these particles here as model nanoparticles because we have to optimize many intermediates and transition states. Also, the use of Pt_{55} and

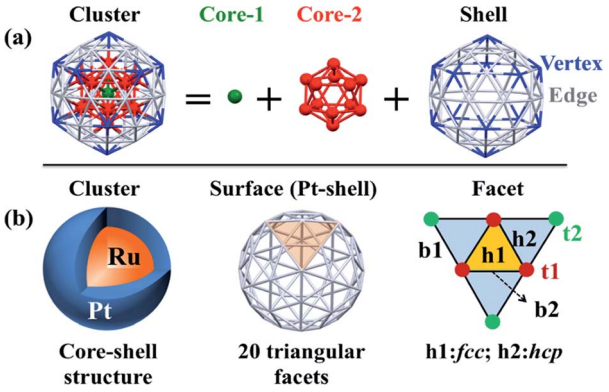

Scheme 1 (a) Geometry of the icosahedron (I_h) 55-atom particle and (b) binding sites of the Pt_{42} shell of the I_h Ru_{13}@Pt_{42} core–shell particle.

Ru_{13}@Pt_{42} particles is not unreasonable, considering that subnanometer-scale metal particles with 55 metal atoms have been employed as model particle in theoretical studies of O_2 adsorption and O–O bond cleavage[46,60–63] and other catalytic reactions.[64–69] The number "55" is a magic number for icosahedral (I_h) and cuboctahedral (O_h) structures. Here, we employed the I_h-like structure because the I_h structure is more stable than O_h in Ru_{13}@Pt_{42}; the relative stabilities of various spin states and comparison between core–shell and non-core–shell structures have been investigated recently.[47] As shown in Scheme 1, the Pt_{42} surface of icosahedral Pt_{55} and Ru_{13}@Pt_{42} consists of 20 triangular facets. Each facet has three different types of binding sites: top (t), bridge (b) and hollow (h). Adsorptions at these binding sites are classified as follows: (i) adsorption at the top site is denoted as t1 or t2, in which the adsorbate binds with one Pt atom at the edge or the vertex position. (ii) Adsorption in a bridging manner is denoted as b1 or b2, in which the adsorbate binds with two adjacent Pt atoms at either the edge and vertex positions or two adjacent edge positions. (iii) Adsorption at the hollow site is denoted as h1 or h2, in which the adsorbate binds at either the fcc-like position among three edge-Pt atoms or the hcp-like position among two edge-Pt atoms and one vertex-Pt atom. We explored all these possible adsorption sites.

3. Results and discussion

In this work, we firstly discuss O_2 adsorption to Pt_{55} and Ru_{13}@Pt_{42}, followed by O–O bond cleavage, OOH formation from the adsorbed O_2 molecule, and O–OH bond cleavage on the Pt_{55} and Ru_{13}@Pt_{42} surfaces. Next, we show the differences in reactivity between Pt_{55} and Ru_{13}@Pt_{42} in these reactions and elucidate the reasons for the differences. Lastly, we unveil the characteristic feature(s) of Ru_{13}@Pt_{42} in comparison with Pt_{55}.

3.1 Dioxygen (O_2) adsorption

The binding energy $E_b(O_2)$ of dioxygen molecule (O_2) increases (becomes more negative) following the order O_2-η^1/h1 < O_2-η^1/t1 < O_2-η^1/t2 < O_2-μ_2/b2 < O_2-μ_3/h2 < O_2-μ_3/h1 < O_2-μ_2/b1 for pure Pt_{55} and O_2-η^1/h1 < O_2-μ_2/b2 < O_2-η^1/t1 < O_2-μ_3/h2 < O_2-μ_3/h1 <

O_2-η^1/t2 < O_2-μ_2/b1 for $Ru_{13}@Pt_{42}$, as shown in Fig. S1 in the ESI,† where h1, t1 *etc.*, represent the adsorption site shown in Scheme 1 and "A-μ_2/x" represents the interaction of adsorbate A with Pt at the x binding site in a μ_2 manner, hereinafter. Obviously, O_2 is preferentially adsorbed at the b1 site of both Pt_{55} and $Ru_{13}@Pt_{42}$ in a μ_2-side-on manner (O_2-μ_2/b1). This is the most stable O_2 adsorption structure. The coordination number of the surface Pt atom is one of the important factors for stabilization of O_2 adsorption: because the coordination number of the vertex Pt atom is 6 but that of the edge Pt is 7, the O_2 molecule tends to interact with the vertex Pt atom compared to the edge Pt atom. However, the O_2 molecule cannot interact with two vertex Pt atoms because the vertex Pt is far from the neighboring vertex Pt. Thus, O_2 interacts with one vertex Pt and one edge Pt in a bridging manner, as seen by the O_2-μ_2/b1 structure.

In the most stable O_2-μ_2/b1-binding species (**2**), the O–O distance of $Pt_{55}(O_2)$ $\mathbf{2}^{\mathbf{Pt}}$ is moderately longer than that of $Ru_{13}@Pt_{42}(O_2)$ $\mathbf{2}^{\mathbf{RuPt}}$, and the Pt–O distance of $\mathbf{2}^{\mathbf{Pt}}$ is moderately shorter than that of $\mathbf{2}^{\mathbf{RuPt}}$, as shown in Fig. 1. The E_b(O_2-μ_2/b1) value is −1.85 (−1.70) eV for Pt_{55} and −1.07 (−0.95) eV for $Ru_{13}@Pt_{42}$, as shown in Fig. 2, where the figures in parentheses represent the binding energy in gas phase. The larger binding energy of the O_2 molecule with Pt_{55} than with $Ru_{13}@Pt_{42}$ is consistent with such geometrical features as the shorter Pt–O and longer O–O distances in $\mathbf{2}^{\mathbf{Pt}}$ than in $\mathbf{2}^{\mathbf{RuPt}}$. The reasons for the stronger O_2 adsorption with Pt_{55} than with $Ru_{13}@Pt_{42}$ are discussed below. It is also noted that solvation by water enhances O_2 binding with these metal particles.

3.2 O–O bond cleavage

Starting from $\mathbf{2}^{\mathbf{Pt}}$ and $\mathbf{2}^{\mathbf{RuPt}}$, O–O bond cleavage occurs *via* transition states **TS2/3a**$^{\mathbf{Pt}}$ and **TS2/3a**$^{\mathbf{RuPt}}$ to afford $Pt_{55}(O)_2$ $\mathbf{3a}^{\mathbf{Pt}}$ and $Ru_{13}@Pt_{42}(O)_2$ $\mathbf{3a}^{\mathbf{RuPt}}$, respectively, as shown in Fig. 1. In **TS2/3a**$^{\mathbf{Pt}}$, the O–O distance is considerably elongated to 1.835 Å, by 0.451 Å, and the Pt–O distances become shorter to 1.825 Å and 1.845 Å, by 0.144 and 0.152 Å (Fig. 1). In **TS2/3a**$^{\mathbf{RuPt}}$, the O–O distance is more elongated to 1.939 Å (by 0.565 Å) than in **TS2/3a**$^{\mathbf{Pt}}$, indicating that **TS2/3a**$^{\mathbf{Pt}}$ is more reactant-like than **TS2/3a**$^{\mathbf{RuPt}}$. Consistent with the O–O bond elongation, the Pt–O distances become shorter in **TS2/3a**. Though they are almost the same between **TS2/3a**$^{\mathbf{Pt}}$ and **TS2/3a**$^{\mathbf{RuPt}}$, the average of Pt–O distances is moderately shorter in $\mathbf{3a}^{\mathbf{Pt}}$ than in $\mathbf{3a}^{\mathbf{RuPt}}$, suggesting the stronger binding energy of the O atom with Pt_{55} than with $Ru_{13}@Pt_{42}$, as discussed below. The activation barrier (E_a) relative to **2** is 0.31 (0.33) eV and 0.35 (0.49) eV for **TS2/3a**$^{\mathbf{Pt}}$ and **TS2/3a**$^{\mathbf{RuPt}}$, respectively, and the reaction energy (ΔE) relative to **2** is −0.90 (−0.83) eV and −0.95 (−0.85) eV, for $\mathbf{3a}^{\mathbf{Pt}}$ and $\mathbf{3a}^{\mathbf{RuPt}}$, as shown in Fig. 2, where a negative ΔE value represents exothermicity. The smaller E_a for the O–O bond cleavage on Pt_{55} than on $Ru_{13}@Pt_{42}$ is consistent with the more reactant-like **TS2/3a**$^{\mathbf{Pt}}$ than **TS2/3a**$^{\mathbf{RuPt}}$. The moderately smaller ΔE in the Pt_{55} case than in the $Ru_{13}@Pt_{42}$ case is seemingly inconsistent with the smaller E_a of the former case than in the latter. But, this is not unreasonable because the O_2 binding energy with Pt_{55} is overly larger than that with $Ru_{13}@Pt_{42}$. It is noted that the E_a is smaller and ΔE is more negative in water than in gas phase, because CT is generally enhanced by polar solvents.

The short Pt–Pt distance of the surface has been discussed as one important factor for high catalytic activity.[70–73] The surface

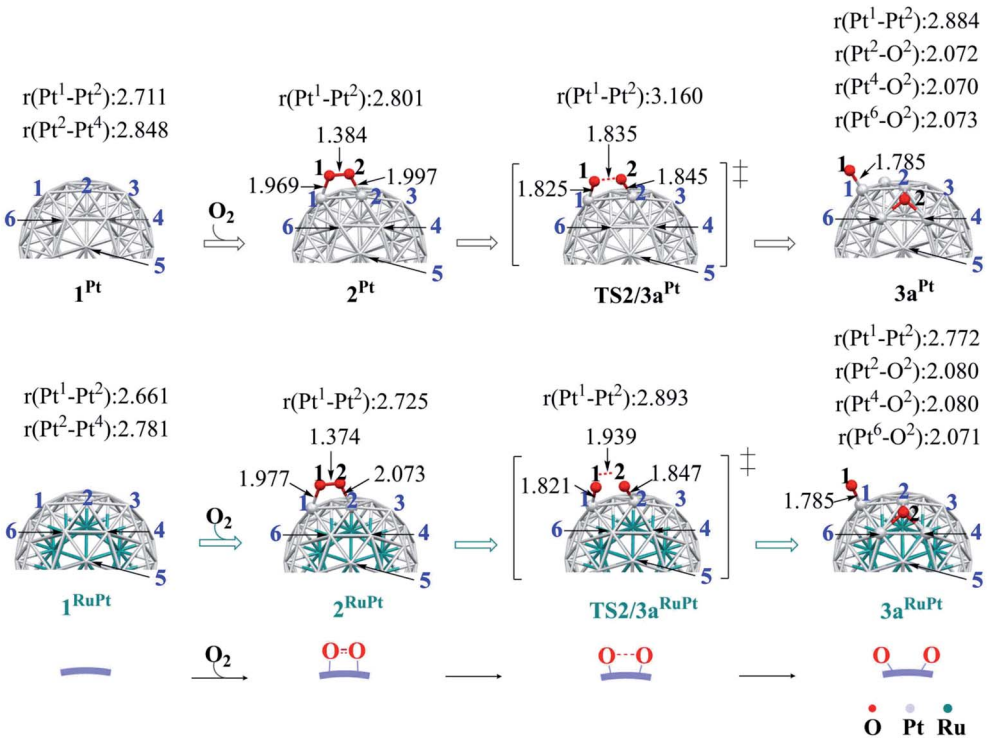

Fig. 1 Geometry changes in O_2 adsorption followed by O–O bond cleavage on Pt_{55} and $Ru_{13}@Pt_{42}$. Values represent bond distance in angstrom.

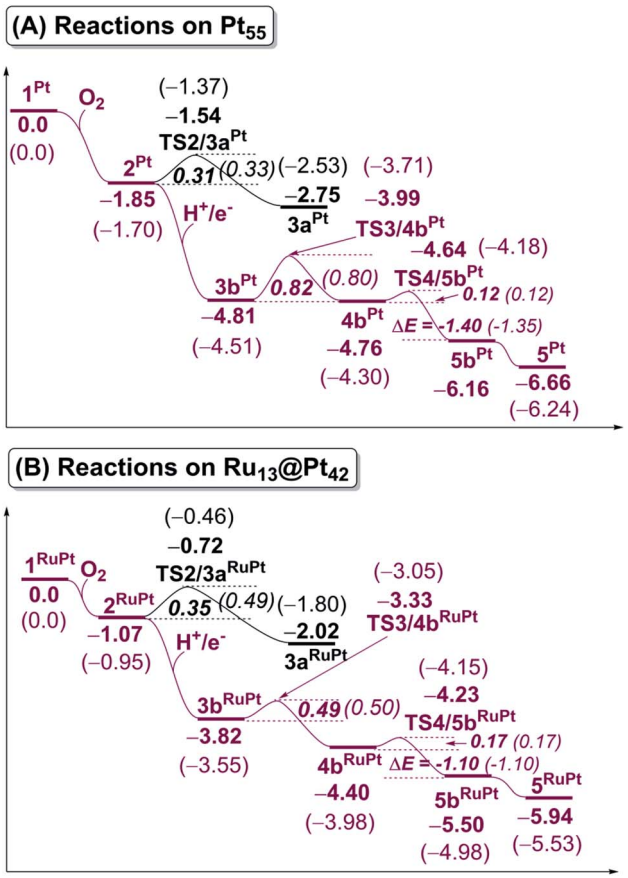

Fig. 2 Energy changes in O_2 adsorption followed by O–O bond cleavage and OOH formation, followed by O–OH bond cleavage, on (A) Pt_{55} and (B) $Ru_{13}@Pt_{42}$. Values represent energy (in eV) relative to Pt_{55} or $Ru_{13}@Pt_{42}$. In parentheses are values for energy in gas phase.

Pt^1–Pt^2 distance becomes longer by the O_2 adsorption and the O–O bond cleavage in both Pt_{55} and $Ru_{13}@Pt_{42}$ (Fig. 1), suggesting that the short Pt–Pt distance of the surface is not beneficial to these processes. The other important factor is flexibility of the Pt surface. Actually, the energy destabilization of Pt_{55} is much smaller than that of $Ru_{13}@Pt_{42}$ when surface Pt–Pt distance is elongated; it is 1.0 kcal mol^{-1} in Pt_{55} and 7.5 kcal mol^{-1} in $Ru_{13}@Pt_{42}$ for the Pt–Pt elongation by 0.4 Å, where we employed rather arbitrarily the elongation of 0.4 Å because the Pt–Pt distance is elongated by about 0.3–0.4 Å at **TS2/3a^{Pt}** of the O–O bond cleavage on Pt_{55}. These results suggest that the longer Pt–Pt distance and the larger flexibility of Pt_{55} than those of $Ru_{13}@Pt_{42}$ are favorable for O_2 adsorption and O–O bond cleavage; in other words, the discussion that short Pt–Pt distance is good for high catalytic activity is not useful when these processes are rate-determining. In addition, it should be noted that the flexibility of the Pt surface is a crucially important factor besides Pt–Pt distance.

3.3 OOH formation followed by O–OH bond cleavage

In ORR, it is likely that the proton is adsorbed easily to the cathode surface because protons exist in excess in solution. Also, electrons are always supplied to the cathode. These features suggest that H species is formed on the cathode surface. Actually, the reactions of adsorbed H atoms with oxygen-containing species were discussed in recent works,[25,74–76] which indicate they correspond to the Langmuir–Hinshelwood pathway. First, we investigated the formation of OOH species from the adsorbed O_2 molecule and H atom on the surface; the adsorption sites of OOH and H are shown in Fig. S3, Tables S2 and S3 in the ESI.†

The H^+/e^- addition occurs with significant exothermicity in **2^{Pt}** and **2^{RuPt}** to afford $Pt_{55}(O_2)(H^1)$ **3b^{Pt}** and $Ru_{13}@Pt_{42}(O_2)(H^1)$ **3b^{RuPt}**, as shown in Fig. 2, where one-half of ΔE of the eq. $2H^+ + 2e^- \rightarrow H_2$, was taken as the energy of H^+/e^-; it is noted that this step can be tuned experimentally by the cell voltage. In **3b^{Pt}** and **3b^{RuPt}**, H^1 takes the position bridging two Pt atoms, as shown in Fig. 3 and 4. Starting from **3b^{Pt}** and **3b^{RuPt}**, the H^1 reacts with the adsorbed O_2 *via* transition states **TS3/4b^{Pt}** and **TS3/4b^{RuPt}** to afford an OOH species adsorbed on the Pt surface $Pt_{55}(OOH)$ **4b^{Pt}** and $Ru_{13}@Pt_{42}(OOH)$ **4b^{RuPt}**, respectively (Fig. 3 and 4). In the transition state, the H^1 is approaching the O^2, keeping a bonding interaction with one Pt, and simultaneously, the O^2 is leaving the Pt_{42} surface. Though the Pt–O^2 distance is very long in **TS3/4b^{Pt}**, the O^2–H^1 distance is still long (1.414 Å), and the O^1–O^2 distance is moderately elongated. In **TS3/4b^{RuPt}**, the O^2–H^1 distance is much longer (2.006 Å) than that of **TS3/4b^{Pt}**, suggesting that **TS3/4b^{RuPt}** is more reactant-like than **TS3/4b^{Pt}**, in contrast to the more product-like **TS2/3a^{RuPt}** than **TS2/3a^{Pt}**. This contrast is reasonable according to the Hammond rule because the O–O bond cleavage occurs with smaller E_a (relative to **2^{Pt}**), but the OOH formation occurs with larger E_a on Pt_{55} than on $Ru_{13}@Pt_{42}$. In **4b^{Pt}** and **4b^{RuPt}**, the O^1–O^2 distance is 1.451 Å and 1.456 Å, respectively, which is moderately shorter than that (1.471 Å, the PBE-D3-optimized value) of free HOOH. The surface Pt^1–Pt^2 distance becomes longer in this reaction, suggesting that the short Pt–Pt distance of the Pt surface is not favorable for this step, either.

We explored here another OOH formation pathway in which adsorbed O_2 molecule undergoes protonation followed by one-electron reduction, as proposed by several works.[77–79] This reaction corresponds to the Eley–Rideal pathway. We compared the energy change in this pathway with that of the Langmuir–Hinshelwood pathway, as shown in Scheme 2. In the Pt_{55} case, the energy changes differ little between these two pathways, suggesting that the OOH formation occurs *via* both pathways. In $Ru_{13}@Pt_{42}$, the H^+/e^- addition to the adsorbed O_2 molecule is more exothermic than that to the Pt_{42} surface (Scheme 2), indicating that the Eley–Rideal pathway is more favorable than the Langmuir–Hinshelwood pathway from the viewpoint of reaction energy. Also, Scheme 2 strongly suggests that the OOH formation occurs more easily on $Ru_{13}@Pt_{42}$ *via* the Eley–Rideal pathway than that on Pt_{55} *via* both the Langmuir–Hinshelwood and Eley–Rideal pathways. Here, we need to mention that the reaction pathway significantly depends on the coverage of Pt surface by O_2 molecules; the Langmuir–Hinshelwood pathway preferentially occurs at low coverage. On the other hand, the Eley–Rideal pathway preferentially occurs at high coverage from the viewpoint of possibility, while the Eley–Rideal pathway becomes less easy at high coverage than at low coverage, from

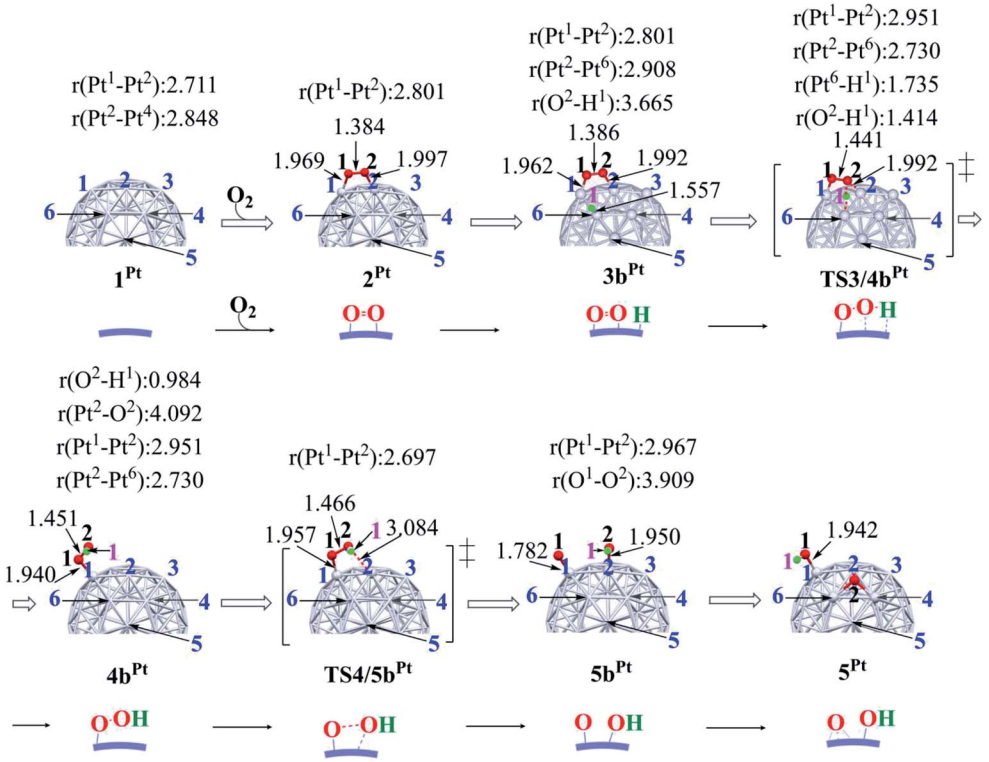

Fig. 3 Geometry changes in OOH formation through the reaction between adsorbed O_2 molecule and H atom, followed by O–OH bond cleavage on Pt_{55} particle. Numbers represent bond distance in angstrom.

the viewpoint of reactivity of adsorbed O_2 molecule, because the adsorbed O_2 molecule becomes less negatively charged at high coverage. The mechanism of OOH formation significantly depends on reaction conditions, which must be investigated carefully in the near future. In both pathways, it is reasonably concluded that OOH formation is an easy process on Pt_{55} and $Ru_{13}@Pt_{42}$ particles.

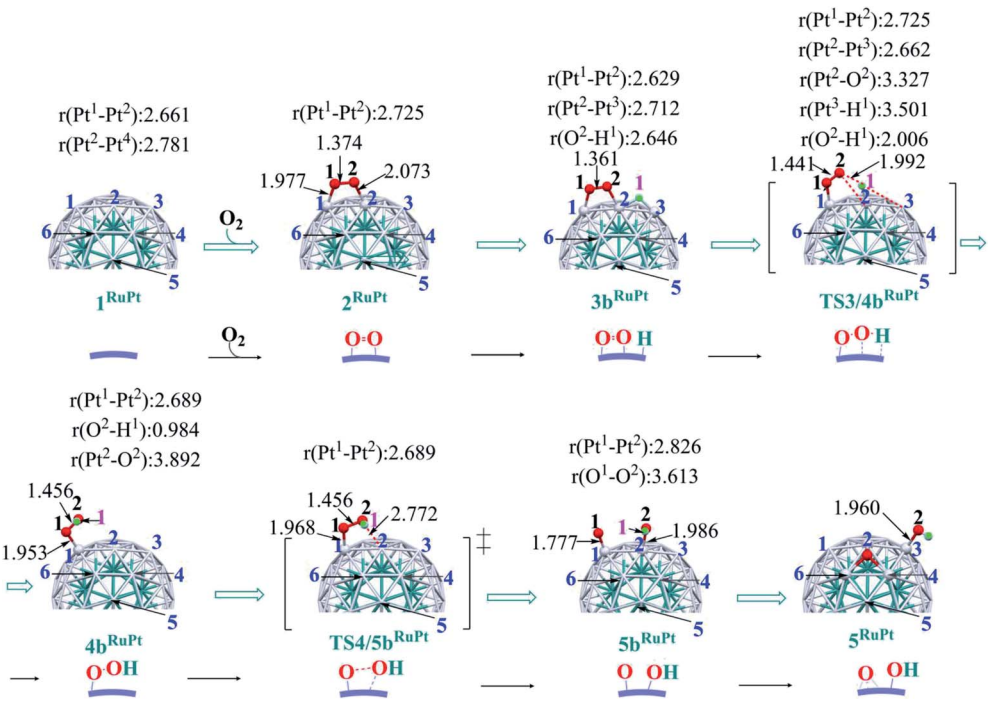

Fig. 4 Geometry changes in OOH formation through the reaction between adsorbed O_2 molecule and H atom, followed by O–OH bond cleavage on $Ru_{13}@Pt_{42}$ particle. Numbers represent bond distance in angstrom.

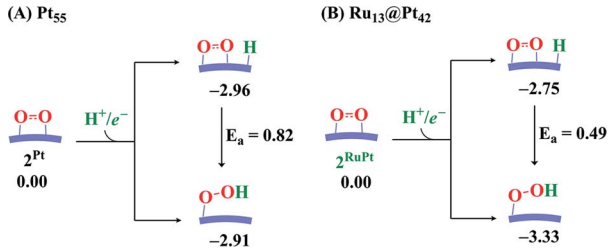

Scheme 2 Comparison of energy change between H^+/e^- addition to the Pt_{42} surface (the Langmuir–Hinshelwood pathway) and the adsorbed O_2 molecule (the Eley–Rideal pathway).

Table 1 Changes of the Bader charges in O_2 adsorption and O–O bond cleavage[a]

	2	TS2/3a	3a
Pt_{55}			
O^1	−0.305 (−0.273)[b]	−0.496 (−0.434)	−0.610 (−0.509)
O^2	−0.300 (−0.259)	−0.480 (−0.406)	−0.706 (−0.684)
Pt_{55}	+0.605 (+0.532)	+0.976 (+0.840)	+1.316 (1.193)
Δ(CT)[c]	0.0 (0.0)	0.371 (0.308)	0.711 (0.661)
$Ru_{13}@Pt_{42}$			
O^1	−0.326 (−0.289)	−0.519 (−0.445)	−0.640 (−0.536)
O^2	−0.320 (−0.268)	−0.506 (−0.427)	−0.719 (−0.689)
$Ru_{13}@Pt_{42}$	+0.646 (+0.557)	+1.025 (0.872)	+1.359 (+1.225)
Δ(CT)[c]	0.0 (0.0)	0.379 (0.315)	0.713 (0.668)

[a] A positive value represents positive atomic charge, and *vice versa*. [b] Values in parentheses represent the Bader charge in gas phase. [c] A positive value represents the increase in charge transfer from the metal particle to O^1 and O^2 atoms.

Starting from **4b^{Pt}** and **4b^{RuPt}**, the O–OH bond is cleaved through transition states **TS4/5b^{Pt}** and **TS4/5b^{RuPt}** to afford Pt_{55}(O)(OH) **5b^{Pt}** and $Ru_{13}@Pt_{42}$(O)(OH) **5b^{RuPt}**, respectively (Fig. 3 and 4). In the transition state, the O^2 is approaching the Pt^2, while the Pt^2–O^2 distance is still long, and the O^1–O^2 distance changes little from those in **4b^{Pt}** and **4b^{RuPt}**, indicating that the transition state is reactant-like. These transition states differ little from each other except for moderately different Pt–O^2 and O^1–O^2 distances.

The OOH formation from adsorbed O_2 and H species occurs with a smaller E_a of 0.49 (0.50) eV on $Ru_{13}@Pt_{41}$ than on Pt_{55} (E_a = 0.82 (0.80) eV), as shown in Fig. 2. The smaller E_a in the reaction on $Ru_{13}@Pt_{42}$ than on Pt_{55} is consistent with the more reactant-like **TS3/4b^{RuPt}** than **TS3/4b^{Pt}**. The O–OH bond cleavage occurs with a very small E_a on both Pt_{55} (E_a = 0.12 (0.12) eV) and $Ru_{13}@Pt_{41}$ (E_a = 0.17 (~0) eV; Fig. 2). The very small E_a for the O–OH bond cleavage is consistent with the reactant-like transition states **TS4/5b^{Pt}** and **TS4/5b^{RuPt}**. Though the E_a is moderately smaller in the reaction on Pt_{55} than on $Ru_{13}@Pt_{42}$, the difference is small, and therefore, the geometry of **TS4/5b^{Pt}** differs little from that of **TS4/5b^{RuPt}**.

It should be noted that the O–OH bond cleavage occurs with a smaller E_a than the O–O bond cleavage of the adsorbed O_2 molecule on both Pt_{55} and $Ru_{13}@Pt_{42}$. This is not surprising because the O–O bond of the adsorbed O_2 molecule is weaker than the original O–O double bond of free O_2 molecule, as shown by the elongated O–O bond, but still stronger than the O–O single bond of the OOH species. Another result to be noted is that the E_a of the OOH formation from adsorbed O_2 and H species is larger in the Pt_{55} case than in the $Ru_{13}@Pt_{42}$ case, but the E_a for O–O bond cleavage is smaller in the Pt_{55} case than in the $Ru_{13}@Pt_{42}$ case. These findings are discussed below in more detail on the basis of electronic structure.

3.4 Electronic process in O_2 adsorption, O–O bond cleavage, OOH formation, and O–OH bond cleavage

As shown in Table 1, the O_2 moiety is negatively charged in $Pt_{55}(O_2)$ **2^{Pt}** and $Ru_{13}@Pt_{42}(O_2)$ **2^{RuPt}**, because O_2 adsorption occurs with charge-transfer (CT) from metal particle to O_2 molecule. This CT is enhanced by the polar solvent (water), as expected. Notably, the O_2 molecule is more negatively charged in **2^{RuPt}** than in **2^{Pt}**. Seemingly, this result is inconsistent with the larger adsorption energy of the O_2 molecule with Pt_{55} than with $Ru_{13}@Pt_{42}$, which is discussed below. In the O–O bond cleavage (**2** → **3a**), both O^1 and O^2 atoms become much more negatively charged, as well known. A moderately larger CT

Table 2 Changes of the Bader charges in OOH formation from adsorbed O_2 and H species and O–OH bond cleavage

	3b	TS3/4b	4b	TS4/5b	5b
Pt_{55}					
O^1	−0.295 (−0.263)[a]	−0.246 (−0.218)	−0.371 (−0.339)	−0.669 (−0.630)	−1.016 (−0.935)
O^2	−0.289 (−0.250)	−0.252 (−0.197)	−0.624 (−0.575)	−0.384 (−0.349)	−0.615 (−0.511)
H	−0.035 (−0.037)	0.198 (0.204)	0.683 (0.609)	0.727 (0.653)	0.676 (0.610)
Pt_{55}	0.619 (0.550)	0.300 (0.211)	0.312 (0.305)	0.326 (0.326)	0.955 (0.836)
$Ru_{13}@Pt_{42}$					
O^1	−0.312 (−0.261)	−0.260 (−0.235)	−0.401 (−0.367)	−0.945 (−0.671)	−1.182 (−1.138)
O^2	−0.278 (−0.245)	−0.210 (−0.140)	−0.800 (−0.728)	−0.401 (−0.367)	−0.708 (−0.680)
H	0.008 (0.007)	0.069 (0.083)	0.872 (0.782)	1.000 (0.675)	0.822 (0.789)
$Ru_{13}@Pt_{42}$	0.582 (0.499)	0.401 (0.292)	0.329 (0.313)	0.346 (0.363)	1.068 (1.029)

[a] Values in parentheses represent the Bader charge in gas phase.

occurs unexpectedly in $Ru_{13}@Pt_{42}$ than in Pt_{55}, despite the larger E_a in $Ru_{13}@Pt_{42}$ than in Pt_{55}.

In the OOH formation *via* the reaction between the adsorbed O_2 molecule and H atom (**3b** → **TS3/4b** → **4b**), the H atom becomes more positively charged, the O^1 and O^2 atoms become more negatively charged, and the positive charges of Pt_{55} and $Ru_{13}@Pt_{42}$ decrease. However, these population changes are not simple. The positive charges of Pt_{55} and $Ru_{13}@Pt_{42}$ decrease when going from **3b** to **TS3/4b** but change little after **TS3/4b**, suggesting that the CT from O_2 and H to the metal particle mostly occurs in step **3b** → **TS3/4b** but little after **TS3/4b**. In this **3b** → **TS3/4b** step, the H atomic charge becomes considerably positive, but the O^1 and O^2 atomic charges moderately change, suggesting that the H atom mainly participates in the CT to the metal particle. As it goes from **TS3/4b** to **4b**, the O^1 becomes more negatively charged, the O^2 is much more negatively charged, and the H atom becomes much more positively charged. Because the CT occurs little to metal particle in this step (**TS3/4b** → **4b**), as discussed above, the change in electron distribution mainly occurs in the O^2H moiety, suggesting that the $O^{\delta-}$–$H^{\delta+}$ polarization becomes strong in this step. It is noted that the positive charges of Pt_{55} and $Ru_{13}@Pt_{42}$ change to a lesser extent in this OOH formation than in the O_2 adsorption, O–O bond cleavage, and O–OH bond cleavage, as shown in Tables 1 and 2. These features suggest that not only CT but also some other factors play important roles in this OOH formation, as discussed below.

In the O^1–O^2H bond cleavage (**4b** → **TS4/5b** → **5b**), the O^2H group becomes considerably positive at **TS4/5b** and then returns to moderately positive at **5b**, while the negative charge of the O^1 atom and the positive charges of Pt_{55} and $Ru_{13}@Pt_{42}$ increase when going from **4b** to **5b**. These population changes indicate that this step occurs with CT from the metal particle to the OOH moiety. These population changes resemble those by the oxidative addition in organometallic chemistry.[80] This is reasonable because the σ-bond cleavage needs CT from the metal to the σ*-antibonding orbital. Because the CT deeply relates to the electronic structure of the metal particle, the next task is to elucidate the electronic structures of Pt_{55} and $Ru_{13}@Pt_{42}$.

3.5 Electronic structures of Pt_{55} and $Ru_{13}@Pt_{42}$, M–X bond energy (M = Pt_{55} and $Ru_{13}@Pt_{42}$; X = H, O, OH, and OOH), and their relation to O_2 activation

The 5d-valence band-top and d-band center of the Pt_{42} shell are calculated at higher energy in Pt_{55} than in $Ru_{13}@Pt_{42}$, but the d-conduction band-bottom of the Pt_{42} shell is calculated at lower energy in Pt_{55} than in $Ru_{13}@Pt_{42}$ (Fig. 5A and B), where the d-band center was calculated using d-valence bands and the DOS energy was corrected according to Baldereschi and coworkers.[81] We checked if the box size for periodic calculation

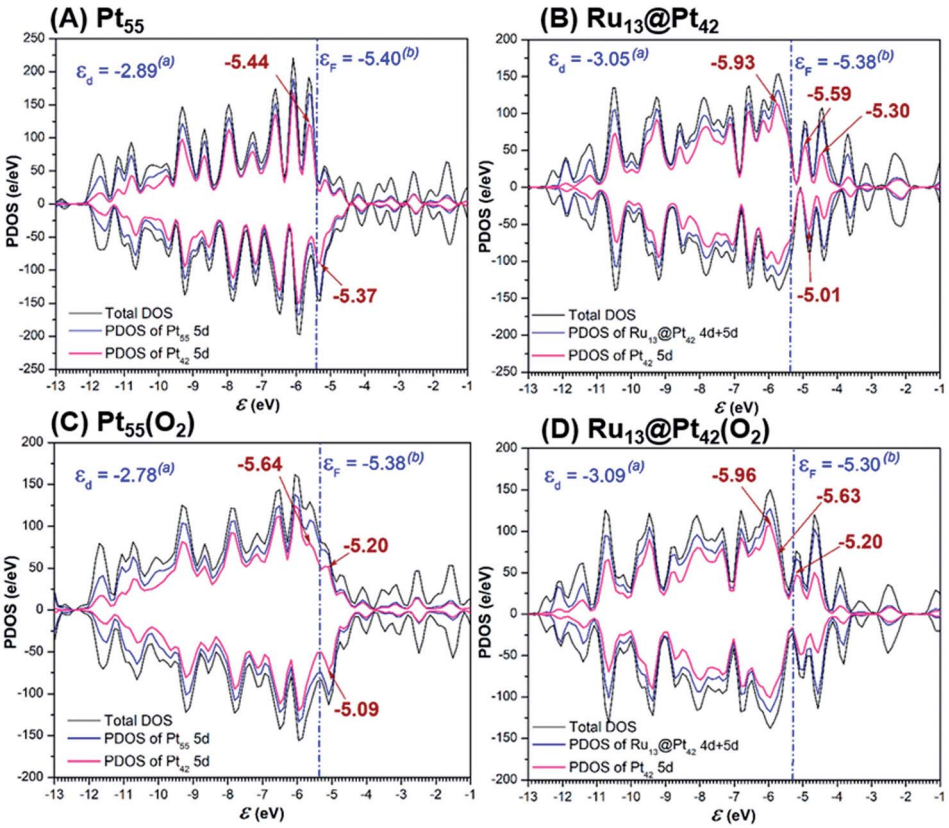

Fig. 5 Density of states (DOS), partial density of states (PDOS) of total d of whole particle and 5d of the Pt_{42} shell in (A) Pt_{55}, (B) $Ru_{13}@Pt_{42}$, (C) $Pt_{55}(O_2)$, and (D) $Ru_{13}@Pt_{42}(O_2)$.

influences little the Fermi level after the correction, as shown in Table S4 in the ESI (page S10†), and also we wish to note the 5d-valence band-top energy differs moderately from that of our previous work,[47] because of the different computation method, as explained in the ESI (pages S11 to S12†). The O_2 adsorption decreases the density of the d-valence band-top and that of the d-conduction band-bottom in both Pt_{55} and $Ru_{13}@Pt_{42}$, as shown by Fig. 5A, B and C, D, indicating that the d-valence band-top mainly participates in the CT from the Pt_{42} shell to the O_2, and the d-conduction band-bottom mainly participates in the reverse CT from the O_2 to the Pt_{42} shell. The higher energy d-valence band-top and the lower energy d-conduction band-bottom induce stronger CT from Pt_{55} to O_2 than that from $Ru_{13}@Pt_{42}$ to O_2 and, also, stronger CT from O_2 to Pt_{55} than that from O_2 to $Ru_{13}@Pt_{42}$, respectively. Consequently, the binding energy of O_2 molecule with Pt_{55} is larger than that with $Ru_{13}@Pt_{42}$, as discussed above, but the O_2 moiety is less negatively charged in $Pt_{55}(O_2)$ than in $Ru_{13}@Pt_{42}(O_2)$; see Table 1. As shown in Fig. 5C and D, the d-valence band-top and d-band center exist at higher energy in $Pt_{55}(O_2)$ than in $Ru_{13}@Pt_{42}(O_2)$. The higher energy d-valence band-top and d-band center in $Pt_{55}(O_2)$ than in $Ru_{13}@Pt_{42}(O_2)$ are the origin of the smaller E_a value of the O–O bond cleavage on Pt_{55} than on $Ru_{13}@Pt_{42}$. Considering these results, we mainly employ the d-valence band-top and the conduction band-bottom for discussion; these DOSs correspond to HOMO and LUMO in the frontier orbital theory in molecular theory. Also, we used the d-band center for discussion because it is an important property representing the electronic structure of metal particles.

In OOH formation, on the other hand, the charge distribution changes to a lesser extent than in the O–O bond cleavage, as mentioned above, but the E_a value is considerably different between Pt_{55} and $Ru_{13}@Pt_{42}$. This result suggests that some different factor plays an important role in this reaction. One plausible factor is bond dissociation energy (BDE). In OOH formation, M–O_2 and M–H bonds are broken and M–(OOH) and O–H bonds are formed, where M represents Pt_{55} and $Ru_{13}@Pt_{42}$. Because the O–H bond formation is common in both Pt_{55} and $Ru_{13}@Pt_{42}$ cases, we focus here on M–O_2, M–H, and M–(OOH) bonds. As shown in Scheme 3, the Pt_{55}–(O_2) and Pt_{55}–H bonds are stronger than the $Ru_{13}@Pt_{42}$–(O_2) and $Ru_{13}@Pt_{42}$–H bonds, respectively, in the reactant side, while the Pt_{55}–(OOH) bond is stronger than the $Ru_{13}@Pt_{42}$–(OOH) bond in the product side. Therefore, two strong Pt_{55}–(O_2) and Pt_{55}–H bonds (the sum of BDEs = 4.48 eV) are converted to one strong Pt_{55}–(OOH) bond (BDE = 1.96 eV) in the OOH formation on Pt_{55}, where the energy loss is 2.52 eV. In the OOH formation on $Ru_{13}@Pt_{42}$, on the other hand, two weaker $Ru_{13}@Pt_{42}$–(O_2) and $Ru_{13}@Pt_{42}$–H bonds (the sum of BDEs = 3.52 eV) are converted to one weaker $Ru_{13}@Pt_{42}$–(OOH) bond (BDE = 1.55 eV), where the energy loss is 1.71 eV. Apparently, the reaction occurs more easily on $Ru_{13}@Pt_{42}$ than on Pt_{55} because of the smaller energy loss in the reaction by the former than by the latter. These results lead us to the conclusion that the stronger Pt_{55}–(O_2) and Pt_{55}–H bonds than $Ru_{13}@Pt_{42}$–(O_2) and $Ru_{13}@Pt_{42}$–H bonds, respectively, are reasons why OOH formation from adsorbed O_2 and H needs a larger E_a on Pt_{55} than on $Ru_{13}@Pt_{42}$.

Because the O–OH bond cleavage needs CT from the metal particle to the OOH moiety, the higher energy d-valence band-top and d-band center of Pt_{55} than those of $Ru_{13}@Pt_{42}$ are the origin of the smaller E_a on Pt_{55} than on $Ru_{13}@Pt_{42}$. In addition, the bond energies relating to this O–OH bond cleavage provide clear understanding of the larger reactivity of Pt_{55} than that of $Ru_{13}@Pt_{42}$, as follows: the Pt_{55}–(OOH) bond is stronger than the $Ru_{13}@Pt_{42}$–(OOH) bond, as shown in Scheme 3, and the Pt_{55}–O and Pt_{55}–(OH) bonds are stronger than the $Ru_{13}@Pt_{42}$–O and $Ru_{13}@Pt_{42}$–(OH) bonds, respectively. This means that one stronger bond is broken, but two stronger bonds are formed in the O–OH bond cleavage by Pt_{55} than by $Ru_{13}@Pt_{42}$. Thus, Pt_{55} is more reactive for this reaction than $Ru_{13}@Pt_{42}$.

As discussed above, the stronger Pt_{55}–(O_2) and Pt_{55}–X bonds (X = H, O, OH, and OOH) than the $Ru_{13}@Pt_{42}$–(O_2) and $Ru_{13}@Pt_{42}$–X bonds, respectively, are responsible for the reactivity difference in OOH formation and O–OH bond cleavage between Pt_{55} and $Ru_{13}@Pt_{42}$. Also, it has been supposed that the overly strong binding energy of oxygen-containing species with the Pt electrode is unfavorable for ORR activity.[17] Thus, it is of considerable importance to discuss the Pt_{55}–X and $Ru_{13}@Pt_{42}$–X bond energies and determining factor of these bond energies. Because the Pt_{55}–(O_2) and $Ru_{13}@Pt_{42}$–(O_2) bond energies were discussed above in terms of the d-valence band-top and d-band center energies, we focus here on Pt_{55}–X and $Ru_{13}@Pt_{42}$–X bond energies. These bonds are neither pure ionic nor pure covalent, but they are understood to be strongly polarized covalent bonds. Polarized covalent bond energy E_{cov} (A–B) is approximately represented by eqn (1) on the basis of simple Hückel MO theory;[82]

$$E_{cov}(A-B) = \sqrt{(\epsilon_A - \epsilon_B)^2 + 4\beta^2}, \quad (1)$$

where ϵ_A and ϵ_B are the valence orbital energies of A and B, respectively, and β is a resonance integral. This eqn (1) has been employed to discuss the relative bond strengths of various M–R bonds (M = transition metal element and R = alkyl, silyl, *etc.*).[83–87] Because the M–R bond is understood to be a polarized covalent bond, it is likely that this eqn (1) can be applied to the present discussion. Actually, this equation has recently been applied to the discussion of binding energies of H, O, and OH species with Pd_{55} and Rh_{55} particles.[66] Eqn (1) indicates that E_{cov} (A–B) becomes larger as the energy difference in valence orbital ($\epsilon_A - \epsilon_B$) increases when the β does not differ. Here, the β value is almost the same between Pt_{55}–X and $Ru_{13}@Pt_{42}$–X because X is bound with the Pt_{42} shell in both particles. Thus, the valence

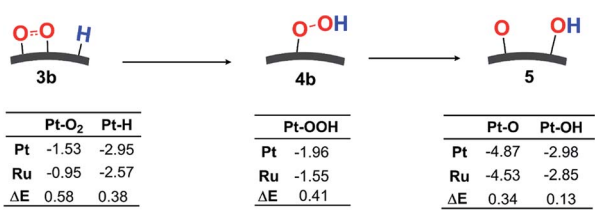

	Pt-O_2	Pt-H
Pt	-1.53	-2.95
Ru	-0.95	-2.57
ΔE	0.58	0.38

	Pt-OOH
Pt	-1.96
Ru	-1.55
ΔE	0.41

	Pt-O	Pt-OH
Pt	-4.87	-2.98
Ru	-4.53	-2.85
ΔE	0.34	0.13

Scheme 3 Bond energy changes (in eV) in OOH formation followed by O–OH bond cleavage on Pt_{55} and $Ru_{13}@Pt_{42}$.

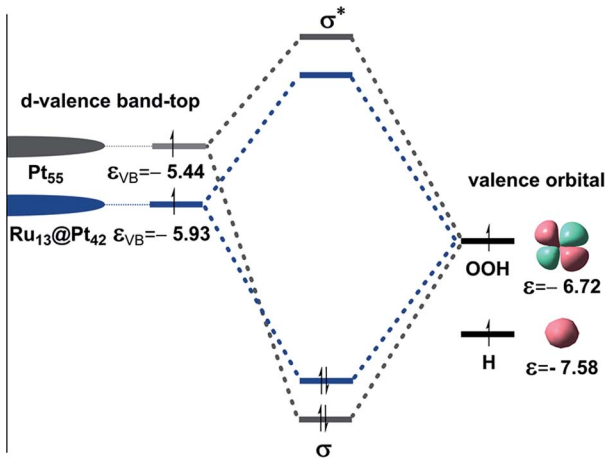

Scheme 4 Schematic representation of orbital interaction between X (X = H or OOH) species and the Pt_{42} shell of Pt_{55} or Ru_{13}@Pt_{42} particle.

orbital energies of Pt_{55} and Ru_{13}@Pt_{42} play an important role in determining these bond energies. As shown in Scheme 4, the d-valence band-top of the Pt_{42} shell is calculated at a higher energy (−5.44 eV) in Pt_{55} than in Ru_{13}@Pt_{42} (−5.93 eV). Because the 2sp valence orbitals of O, OH, and OOH and the 1s valence orbital of H are at lower energy than these d-valence band-tops due to their larger electronegativities, the energy difference between the d-valance band-top of the Pt_{42} shell and the valence orbital of X species is larger in Pt_{55} than in Ru_{13}@Pd_{42}, as apparently shown in Scheme 4; for simplicity, O and OH valence orbitals are omitted in this Scheme. Consequently, the Pt_{55}–X bond is stronger than the Ru_{13}@Pt_{42}–X bond.

It should be clearly concluded that the higher energy d valence band-top of Pt_{55} than that of Ru_{13}@Pt_{42} is the origin of the stronger Pt_{55}–X bond than the Ru_{13}@Pt_{42}–X bond. The higher energy d valence band-top of Pt_{55} than that of Ru_{13}@Pt_{42} is also responsible for the larger O_2 adsorption energy to Pt_{55} than to Ru_{13}@Pt_{42} and smaller E_a values of the O–O and O–OH bond cleavages on Pt_{55} than on Ru_{13}@Pt_{42}. Thus, one of the important characteristic features of Ru_{13}@Pt_{42} is the presence of the d-valence band-top of the Pt_{42} shell at lower energy than that of Pt_{55}; here we wish to mention that higher energy d-valence band-top relates to higher energy d-band center in many cases, indicating that the d-band center is also useful for discussion.

4 Conclusions

O_2 adsorption followed by O–O bond cleavage and OOH formation followed by O–OH bond cleavage on Pt_{55} and Ru_{13}@Pt_{42} particles were investigated using DFT computations, and comparisons were made between Pt_{55} and Ru_{13}@Pt_{42}. Several important findings are summarized as follows: (i) O_2 is preferentially adsorbed to the vertex Pt and the neighboring edge Pt atoms in a bridging μ_2-side-on manner. (ii) The O_2 adsorption energy with the Pt_{42} shell is larger in Pt_{55} than in Ru_{13}@Pt_{42}. (iii) The O–O bond cleavage occurs with a smaller E_a on Pt_{55} than on Ru_{13}@Pt_{42}. (iv) The OOH formation from the adsorbed O_2 molecule and H atom occurs with a smaller E_a on Ru_{13}@Pt_{42} than on Pt_{55}. The CT occurs much less in this reaction than in the O–O bond cleavage. The stronger Pt_{55}–(O_2) and Pt_{55}–H bonds than the Ru_{13}@Pt_{42}–(O_2) and Ru_{13}@Pt_{42}–H bonds, respectively, are the origin of the larger E_a on Pt_{55} than on Ru_{13}@Pt_{42}. (v) The OOH formation *via* H^+/e^- addition to the adsorbed O_2 molecule also occurs easily in Pt_{55} similarly to the reaction between adsorbed O_2 molecule and H atom, but more easily in Ru_{13}@Pt_{42}. And, (vi) the O–OH bond cleavage occurs more easily with much smaller E_a than the O–O bond cleavage of the adsorbed O_2 molecule.

The abovementioned differences between Pt_{55} and Ru_{13}@Pt_{42} are understood on the basis of the PDOS of these metal particles. The d-valence band-top and d-band center of the Pt_{42} shell are calculated at higher energy in Pt_{55} than in Ru_{13}@Pt_{42}, but the d-conduction band-bottom of the Pt_{42} shell is at lower energy in Pt_{55} than in Ru_{13}@Pt_{42}. Accordingly, the O_2 molecule is adsorbed to Pt_{55} more strongly than to Ru_{13}@Pt_{42}, because the CT from the Pt_{42} shell to O_2 and the reverse CT from the O_2 to the Pt_{42} shell are more strongly formed with Pt_{55} than with Ru_{13}@Pt_{42}. Because the O–O bond cleavage needs CT from the metal particle to the O_2 moiety, the presence of d-valence band-top at high energy is favorable. Consequently, Pt_{55} is more reactive than Ru_{13}@Pt_{42}. On the other hand, the reactivity for OOH formation from adsorbed O_2 and H depends on the M–(O_2) and M–H bond energies, as follows: because the Pt_{55}–(O_2) and Pt_{55}–H bonds are stronger than the Ru_{13}@Pt_{42}–(O_2) and Ru_{13}@Pt_{42}–H bonds, respectively, OOH formation on Pt_{55} needs a larger E_a than that on Ru_{13}@Pt_{42}.

The binding energy of oxygen-containing species with Pt-based electrode has been discussed as an important factor for ORR activity. Also, the above discussion suggests that the bond energy is an important property for understanding reactions on the Pt-based electrode. We explored the Pt_{55}–X (X = H, O, OH, and OOH) and Ru_{13}@Pt_{42}–X bond energies and found that the Ru_{13}@Pt_{42}–X bond is weaker than the Pt_{55}–X, and the lower energy d-valence band-top of Ru_{13}@Pt_{42} than that of Pt_{55} is the origin of the weaker Ru_{13}@Pt_{42}–X bond than the Pt_{55}–X bond. It is clearly concluded that the lower energy of the d-valence band-top of Ru_{13}@Pt_{42} than that of Pt_{55} is one of the important characteristic features of Ru_{13}@Pt_{42} in comparison to Pt_{55}.

Conflicts of interest

The authors declare no competing financial interest.

Acknowledgements

This work was performed in part with support from the Ministry of Education, Culture, Science, Sports, and Technology (Japan) through the Element Strategy Initiative for Catalysts and Batteries (ESICB) in Kyoto University and from the Ministry of Economy, Trade, and Industry though the New Energy and Industrial Technology Development Organization (NEDO) through a project JPNP16010. We wish to thank the computational center at the Institute for Molecular Science (IMS;

Okazaki, Japan) and High Performance Computation Infrastructure (HPCI; Kobe, Japan) for use of their computers.

Notes and references

1 M. E. Scofield, H. Q. Liu and S. S. Wong, *Chem. Soc. Rev.*, 2015, **44**, 5836–5860.
2 H. L. Liu, F. Nosheen and X. Wang, *Chem. Soc. Rev.*, 2015, **44**, 3056–3078.
3 Y. J. Wang, B. Z. Fang, H. Li, X. T. T. Bi and H. J. Wang, *Prog. Mater. Sci.*, 2016, **82**, 445–498.
4 S. Sui, X. Y. Wang, X. T. Zhou, Y. H. Su, S. Riffatc and C. J. Liu, *J. Mater. Chem. A*, 2017, **5**, 1808–1825.
5 J. P. Lai and S. J. Guo, *Small*, 2017, **13**, 1702156.
6 T. Asset, R. Chattot, M. Fontana, B. Mercier-Guyon, N. Job, L. Dubau and F. Maillard, *ChemPhysChem*, 2018, **19**, 1552–1567.
7 K. Singh, E. B. Tetteh, H. Y. Lee, T. H. Kang and J. S. Yu, *ACS Catal.*, 2019, **9**, 8622–8645.
8 O. Lori and L. Elbaz, *ChemCatChem*, 2020, **12**, 3434–3446.
9 M. Sharma, N. Jung and S. J. Yoo, *Chem. Mater.*, 2018, **30**, 2–24.
10 S. T. Hunt and Y. Roman-Leshkov, *Acc. Chem. Res.*, 2018, **51**, 1054–1062.
11 B. W. Zhang, H. L. Yang, Y. X. Wang, S. X. Dou and H. K. Liu, *Adv. Energy Mater.*, 2018, **8**, 1703597.
12 N. K. Chaudhari, Y. Hong, B. Kim, S. I. Choi and K. Lee, *J. Mater. Chem. A*, 2019, **7**, 17183–17203.
13 X. F. Ren, Q. Y. Lv, L. F. Liu, B. H. Liu, Y. R. Wang, A. M. Liu and G. Wu, *Sustainable Energy Fuels*, 2020, **4**, 15–30.
14 K. Sasaki, K. A. Kuttiyiel and R. R. Adzic, *Curr. Opin. Electrochem.*, 2020, **21**, 368–375.
15 L. J. Yang, M. B. Vukmirovic, D. Su, K. Sasaki, J. A. Herron, M. Mavrikakis, S. J. Liao and R. R. Adzic, *J. Phys. Chem. C*, 2013, **117**, 1748–1753.
16 A. Jackson, V. Viswanathan, A. J. Forman, J. K. Nørskov and T. F. Jaramillo, *ECS Trans.*, 2013, **58**, 929–936.
17 A. Jackson, V. Viswanathan, A. J. Forman, A. H. Larsen, J. K. Nørskov and T. F. Jaramillo, *ChemElectroChem*, 2014, **1**, 67–71.
18 D. Takimoto, T. Ohnishi, J. Nutariya, Z. R. Shen, Y. Ayato, D. Mochizuki, A. Demortiere, A. Boulineau and W. Sugimoto, *J. Catal.*, 2017, **345**, 207–215.
19 A. Jackson, A. L. Strickler, D. Higgins and T. F. Jaramillo, *Nanomaterials*, 2018, **8**, 38.
20 J. S. Zou, M. Wu, S. L. Ning, L. Huang, X. W. Kang and S. W. Chen, *ACS Sustainable Chem. Eng.*, 2019, **7**, 9007–9016.
21 Y. Sha, T. H. Yu, Y. Liu, B. V. Merinov and W. A. Goddard III, *J. Phys. Chem. Lett.*, 2010, **1**, 856–861.
22 T. H. Yu, Y. Sha, B. V. Merinov and W. A. Goddard III, *J. Phys. Chem. C*, 2010, **114**, 11527–11533.
23 Y. Sha, T. H. Yu, B. V. Merinov, P. Shirvanian and W. A. Goddard III, *J. Phys. Chem. Lett.*, 2011, **2**, 572–576.
24 Y. Sha, T. H. Yu, B. V. Merinov, P. Shirvanian and W. A. Goddard III, *J. Phys. Chem. C*, 2012, **116**, 21334–21342.
25 Y. Sha, T. H. Yu, B. V. Merinov and W. A. Goddard III, *ACS Catal.*, 2014, **4**, 1189–1197.
26 A. Fortunelli, W. A. Goddard III, Y. Sha, T. H. Yu, L. Sementa, G. Barcaro and O. Andreussi, *Angew. Chem., Int. Ed.*, 2014, **53**, 6669–6672.
27 H. C. Tsai, T. H. Yu, Y. Sha, B. V. Merinov, P. W. Wu, S. Y. Chen and W. A. Goddard III, *J. Phys. Chem. C*, 2014, **118**, 26703–26712.
28 A. Fortunelli, W. A. Goddard III, L. Sementa, G. Barcaro and F. R. Negreiros, *Chem. Sci.*, 2016, **6**, 3915–3925.
29 A. Fortunelli, W. A. Goddard III, L. Sementa and G. Barcaro, *Nanoscale*, 2015, **7**, 4514–4521.
30 H. C. Tsai, Y. C. Hsieh, T. H. Yu, Y. J. Lee, Y. H. Wu, B. V. Merinov, P. W. Wu, S. Y. Chen, R. R. Adzic and W. A. Goddard III, *ACS Catal.*, 2015, **5**, 1568–1580.
31 L. Sementa, O. Andreussi, W. A. Goddard III and A. Fortunelli, *Catal. Sci. Technol.*, 2016, **6**, 6901–6909.
32 E. Toyoda, R. Jinnouchi, T. Hatanaka, Y. Morimoto, K. Mitsuhara, A. Visikovskiy and Y. Kido, *J. Phys. Chem. C*, 2011, **115**, 21236–21240.
33 X. Liu, L. Li, C. G. Meng and Y. Han, *J. Phys. Chem. C*, 2012, **116**, 2710–2719.
34 L. Zhang, R. Iyyamperumal, D. F. Yancey, R. M. Crooks and G. Henkelman, *ACS Nano*, 2013, **7**, 9168–9172.
35 Z. Chen, X. Zhang and G. Lu, *J. Phys. Chem. C*, 2017, **121**, 1964–1973.
36 T. Ikeshoji and M. Otani, *Phys. Chem. Chem. Phys.*, 2017, **19**, 4447–4453.
37 X. Wang, W. Huang, S. Liao and B. Li, *Mater. Chem. Phys.*, 2018, **212**, 378–384.
38 Y. Wang, Y. F. Li and T. Heine, *J. Am. Chem. Soc.*, 2018, **140**, 12732–12735.
39 J. Huang and M. Eikerling, *Curr. Opin. Electrochem.*, 2019, **13**, 157–165.
40 M. M. Montemore, M. A. van Spronsen, R. J. Madix and C. M. Friend, *Chem. Rev.*, 2018, **118**, 2816–2862.
41 S. Liu and P. Liu, *J. Electrochem. Soc.*, 2018, **165**, J3090–J3094.
42 X. Wang, W. Huang, S. Liao and B. Li, *Mater. Chem. Phys.*, 2018, **212**, 378–384.
43 Y. Zhuang, J.-P. Chou, P.-Y. Liu, T.-Y. Chen, J.-J. Kai, A. Hu and H.-Y. T. Chen, *J. Mater. Chem. A*, 2018, **6**, 23326–23335.
44 A. S. Nair and B. Pathak, *J. Phys. Chem. C*, 2019, **123**, 3634–3644.
45 C. Fu, C. Liu, T. Li, X. Zhang, F. Wang, J. Yang, Y. Jiang, P. Cui and H. Li, *Comput. Mater. Sci.*, 2019, **170**(12), 1092022.
46 Z. Zhao, H. Xu, Z. Feng, Y. Zhang, M. Cui, D. Cao and D. Cheng, *Chem.–Eur. J.*, 2020, **26**, 4128–4135.
47 J. Lu, K. Ishimura and S. Sakaki, *J. Phys. Chem. C*, 2018, **122**, 9081–9090.
48 F. Viñes, J. R. B. Gomesb and F. Illas, *Chem. Soc. Rev.*, 2014, **43**, 4922–4939.
49 S. T. Hunt and Y. Roman-Leshkov, *Acc. Chem. Res.*, 2018, **51**, 1054–1062.
50 J. A. Trindell, Z. Y. Duan, G. Henkelman and R. M. Crooks, *Chem. Rev.*, 2020, **120**, 814–850.
51 G. Kresse and J. Furthmüller, *Comput. Mater. Sci.*, 1996, **6**, 15–50.
52 G. Kresse and J. Furthmüller, *Phys. Rev. B: Condens. Matter Mater. Phys.*, 1996, **54**, 11169–11186.

53 J. P. Perdew, K. Burke and M. Ernzerhof, *Phys. Rev. Lett.*, 1996, **77**, 3865–3868.
54 S. Grimme, J. Antony, S. Ehrlich and H. Krieg, *J. Chem. Phys.*, 2010, **132**, 154104.
55 G. Stefan, E. Stephan and G. Lars, *J. Comput. Chem.*, 2011, **32**, 1456–1465.
56 G. Mills and H. Jónsson, *Phys. Rev. Lett.*, 1994, **72**, 1124–1127.
57 G. Mills, H. Jónsson and G. K. Schenter, *Surf. Sci.*, 1995, **324**, 305–337.
58 K. Mathew, R. Sundararaman, K. Letchworth-Weaver, T. A. Arias and R. G. Hennig, *J. Chem. Phys.*, 2014, **140**, 084106.
59 M. Fishman, H. L. Zhuang, K. Mathew, W. Dirschka and R. G. Hennig, *Phys. Rev. B: Condens. Matter Mater. Phys.*, 2013, **87**, 245402.
60 D. J. Cheng and W. C. Wang, *Nanoscale*, 2012, **4**, 2408–2415.
61 J. H. Shin, J.-H. Choi, Y.-S. Bae and S.-C. Lee, *Chem. Phys. Lett.*, 2014, **610**, 86–90.
62 P. C. Jennings, H. A. Aleksandrov, K. M. Neyman and R. L. Johnston, *Nanoscale*, 2014, **6**, 1153–1165.
63 S. Dobrin, *Phys. Chem. Chem. Phys.*, 2012, **14**, 12122–12129.
64 D. Cheng, H. Xu and A. Fortunelli, *J. Catal.*, 2014, **314**, 47–55.
65 L. Ma and J. Akola, *Phys. Chem. Chem. Phys.*, 2019, **21**, 11351–11358.
66 T. Morishita, T. Ueno, G. Panomsuwan, J. Hieda, M. A. Bratescu and N. Saito, *RSC Adv.*, 2016, **6**, 98091–98095.
67 F. Deushi, A. Ishikawa and H. Nakai, *J. Phys. Chem. C*, 2017, **121**, 15272–15281.
68 N. Takagi, K. Ishimura, R. Fukuda, M. Ehara and S. Sakak, *J. Phys. Chem. A*, 2019, **123**, 7021–7033.
69 B. Zhu, M. Ehara and S. Sakaki, *Phys. Chem. Chem. Phys.*, 2020, **22**, 11783–11796.
70 A. Ruban, B. Hammer, P. Stoltze, H. L. Skriver and J. K. Nørskov, *J. Mol. Catal. A: Chem.*, 1997, **115**, 421–429.
71 J. R. Kitchin, J. K. Nørskov, M. A. Barteau and J. G. Chen, *Phys. Rev. Lett.*, 2004, **93**, 156801.
72 Q. Jia, C. U. Segre, D. Ramaker, K. Caldwell, M. Trahan and S. Mukerjee, *Electrochim. Acta*, 2013, **88**, 604–613.
73 Q. Jia, W. Liang, M. K. Bates, P. Mani, W. Lee and S. Mukerjee, *ACS Nano*, 2015, **9**, 387–400.
74 A. B. Anderson, R. A. Sidik, J. Narayanasamy and P. Shiller, *J. Phys. Chem. B*, 2003, **107**, 4618–4623.
75 Q. Liang, J. Yu and J. Lia, *J. Chem. Phys.*, 2006, **125**, 054701.
76 A. S. Haile, W. Yohannes and Y. S. Mekonnen, *RSC Adv.*, 2020, **10**, 27346–27356.
77 R. A. Sidik and A. B. Anderson, *J. Electroanal. Chem.*, 2002, **528**, 69–76.
78 Y. X. Wang and P. B. Balbuena, *J. Phys. Chem. B*, 2004, **108**, 4376–4384.
79 Y. X. Wang and P. B. Balbuena, *J. Phys. Chem. B*, 2005, **109**, 14896–14907.
80 W. Guan, F. B. Sayyed, G. Zeng and S. Sakaki, *Inorg. Chem.*, 2014, **53**, 6444–6457.
81 C. J. Fall, N. Binggeli and A. Baldereschi, *J. Phys.: Condens. Matter*, 1999, **11**, 2689–2696.
82 S. Sakaki, B. Biswas and M. Sugimoto, *Organometallics*, 1998, **17**, 1278–1289.
83 S. Sakaki, S. Kai and M. Sugimoto, *Organometallics*, 1999, **18**, 4825–4837.
84 B. Biswas, M. Sugimoto and S. Sakaki, *Organometallics*, 1999, **18**, 4015–4026.
85 M. Ray, Y. Nakao, H. Sato and S. Sakaki, *Organometallics*, 2007, **26**, 4413–4423.
86 M. Ray, Y. Nakao, H. Sato, H. Sakaba and S. Sakaki, *Organometallics*, 2009, **28**, 65–73.
87 R. L. Zhong and S. Sakaki, *J. Am. Chem. Soc.*, 2019, **141**, 9854–9866.